



Experimental Investigation on the Slip Nucleation of Laminated Shale During Fracture Propagation

Lei Chen¹ · Guangqing Zhang^{1,2} · Min Zhang¹ · Chaozhao Zhai¹ · Zongyang Fan¹ · Jianlin Zhao^{1,2} · Dawei Zhou^{1,2} · Shiyuan Li^{1,2}

Received: 22 September 2022 / Accepted: 9 January 2023 / Published online: 4 February 2023
© The Author(s), under exclusive licence to Springer-Verlag GmbH Austria, part of Springer Nature 2023

Abstract

Slip usually occurs in the laminated structure of shale formations during hydraulic fracturing. In this paper, we used laminated shale to conduct macro and micro three-point bending experiments, as well as the visual hydraulic fracturing experiment to study the slip nucleation during fracture propagation, where the digital image correlation method (DIC) was used to monitor the interlaminar deformation. Based on the linear slip weakening model, a method to identify the slip nucleation zone (SNZ) using DIC was proposed, which could visually detect the formation of SNZ. In laminated shales from millimeter scale to decimeter scale, two asymmetric slip nucleation zones along the interface were observed on both sides of the opening-mode fracture tip before cohesionless slipping. The dominant path of slip could be predicted from the developed size of the conjugated SNZs. The linear slip weakening model considering the tensile fracture tip opening displacements (w) was discussed, according to which the SNZ length and interlaminar fracture energy would increase with w during quasi-static nucleation. After the cohesionless slipping, the residual slip zone was defined, which should be a part of the hydraulic fracture systems but was ignored in previous research. The findings of this study could help to understand the generation mechanism of slips in shale reservoirs during hydraulic fracturing.

Highlights

- A method for identifying the slip nucleation zone based on digital imaging was proposed.
- Two asymmetric interlaminar SNZs were found on both sides of the opening-mode fracture tip before cohesionless slipping.
- The dominant path of slip could be predicted from the developed size of the conjugated SNZs.
- The residual slip zone should be a part of the hydraulic fracture systems in shale formations.

Keywords Shale · Slip nucleation · Hydraulic fracturing · Slip weakening zone model · Digital image correlation

1 Introduction

Nowadays, conventional oil and gas resources are insufficient to meet energy demands. Since the success of the shale gas revolution in North America, unconventional geological resources such as shale oil and gas have drawn increasing attention around the world (Hu et al. 2020; Yan et al. 2017; Zhang et al. 2021). Due to the low permeability of shale matrix, the production of oil and gas mainly depends on artificial fracture systems (He et al. 2019; Wu et al. 2022; Zhou

✉ Guangqing Zhang
zhangguangqing@cup.edu.cn

¹ Department of Engineering Mechanics, College of Petroleum Engineering, China University of Petroleum, Beijing 102249, China

² State Key Laboratory of Petroleum Resources and Prospecting, China University of Petroleum, Beijing 102249, China

et al. 2022). In field application, hydraulic fracturing of horizontal wells has been widely used for its larger volume of stimulation (Nikolskiy and Lecampion 2020; Saberhosseini et al. 2019). Influenced by the in situ stress, the horizontal wells usually generate vertical opening-mode fractures. Meanwhile, as sedimentary rocks, the shale formations were characterized by lamination development (Pan et al. 2021; Tan et al. 2017). Thus, hydraulic fracture propagation in laminated shale formations has become a research focus (Jia et al. 2021; Lin et al. 2017; Tan et al. 2017; Zou et al. 2016). In particular, the mechanical behaviors of interlaminar slip induced by the opening-mode fracture are the key issues to be discussed (Galybin and Mukhamediev 2014).

The analyses of microseismic monitoring toward in situ fracturing showed that hydraulic fracture (HF) could induce interlaminar slip (Tan & Engelder 2016), which would improve hydraulic conductivity (Zhao et al. 2013). Thus, interlaminar slip is a potential factor promoting the production of shale formations (Zoback et al. 2012). At present, the slip criteria of weak interface proposed by Renshaw and Warpinski et al. (Renshaw and Pollard 1995; Warpinski and Teufel 1987) are widely used to judge the occurrence of interlayer slip. To find the potential slip zone, Zhao and Gray (2021) studied the distributions of the stress field near the weak interface induced by HF based on linear elastic fracture mechanics. However, the related research mainly focused on the estimation of interlaminar slip, ignoring the slip process. Through an innovative hydraulic fracturing experiment, AlTammar and Sharma concluded that shear failure and slippage would be generated along the weak interface during fracture propagation (AlTammar et al. 2019). Some researchers (Garcia et al. 2013; Yaghoubi 2019) also used numerical simulations to study the propagation of hydraulic fractures in shale without discussing the generation mechanism of slip, especially induced by the opening-mode fracture. In fact, similar to the fracture process zone ahead of a cohesionless opening-mode fracture of rock materials (Chen et al. 2020, 2021; Zhang et al. 2018), a development process zone also exists at the weak interface during slip, showing stress softening or weakening in mechanical behaviors. It could be called slip weakening zone or slip nucleation zone (SNZ), referring to the studies about fault slip (Ampuero et al. 2002; Chen & Knopoff 1986; Rice 1979; Uenishi and Rice 2003).

The concept of slip nucleation was systematically introduced by Rice in the study of fault slip (Rice 1979) when discussing the mechanics of earthquake rupture. Subsequently, Segall et al. (Segall and Pollard 1983) described the nucleation process and propagation of granodiorite fault by field observation. As for the constitutive model of SNZ, the slip weakening model was developed to describe the mechanical behaviors of SNZ (Palmer et al. 1973; Rice 1979), which was an extension of the cohesive zone model

from tensile fracture to shear slip (Barenblatt 1962; Hillerborg et al. 1976). The slip weakening model could avoid the problem of stress singularity at the fracture tip, and the constitutive relationship of SNZ can be described by the kinetic and static friction forces and slip displacements. Based on the slip weakening model, Uenishi and Rice investigated the factors influencing the critical length of SNZ and discussed the conditions of dynamic slip (Uenishi and Rice 2003). With regard to the research of SNZ induced by hydraulic fracturing, previous publications mainly focus on the fault slip (Azad et al. 2017; Garagash and Germanovich 2012; Zhang and Jeffrey 2016), ignoring the potential slip nucleation of the interlamination, such as the weak interface. In fact, the presence of SNZ would significantly affect the hydraulic fracture propagation of layered shale, which was neglected in previous studies. The study of SNZ can help to understand the generation of hydraulic fractures and the dissipation of fracture energy during fracturing in laminated shale reservoirs.

In this paper, the macro (specimen in centimeter scale) and micro (specimen in millimeter scale) three-point bending experiments and the visual hydraulic fracturing experiment were carried out using laminated shales with weak interfaces. From the digital imaging technique, a method for identifying the slip nucleation zone was proposed to study the formation mechanism of SNZ during opening-mode fracturing. This study can help to understand the development of hydraulic fractures in laminated shale.

2 Experimental Methods and Results

2.1 Specimens and Experiments

The laminated shale rock from Shaanxi, China was used to conduct the three-point bending experiments (Fig. 1a). As shown in the casting thin section (Fig. 1b), the Shaanxi shale rock was developed with weak interfaces. The argillaceous structures are mainly composed of reticular clay, followed by quartz, feldspar, mica debris, argillaceous iron, kaolinite, chlorite, etc. While the sand is rich of silty quartz and feldspar, with some debris. The pores are represented by interlaminar fractures, occupied by the residual organic matter. The MTS-816 testing system was used to carry out the macro three-point bending (Macro-TPB) experiments on centimeter-scale shale (Fig. 1c) to study the slip nucleation during opening-mode fracturing. As an effective means to study fracture mechanics, the three-point bending experiment could help to understand the mechanical behaviors of fracture initiation and propagation, similar to hydraulic fracturing. Due to the high brittleness of shale, the negative feedback method was used to control the fracture

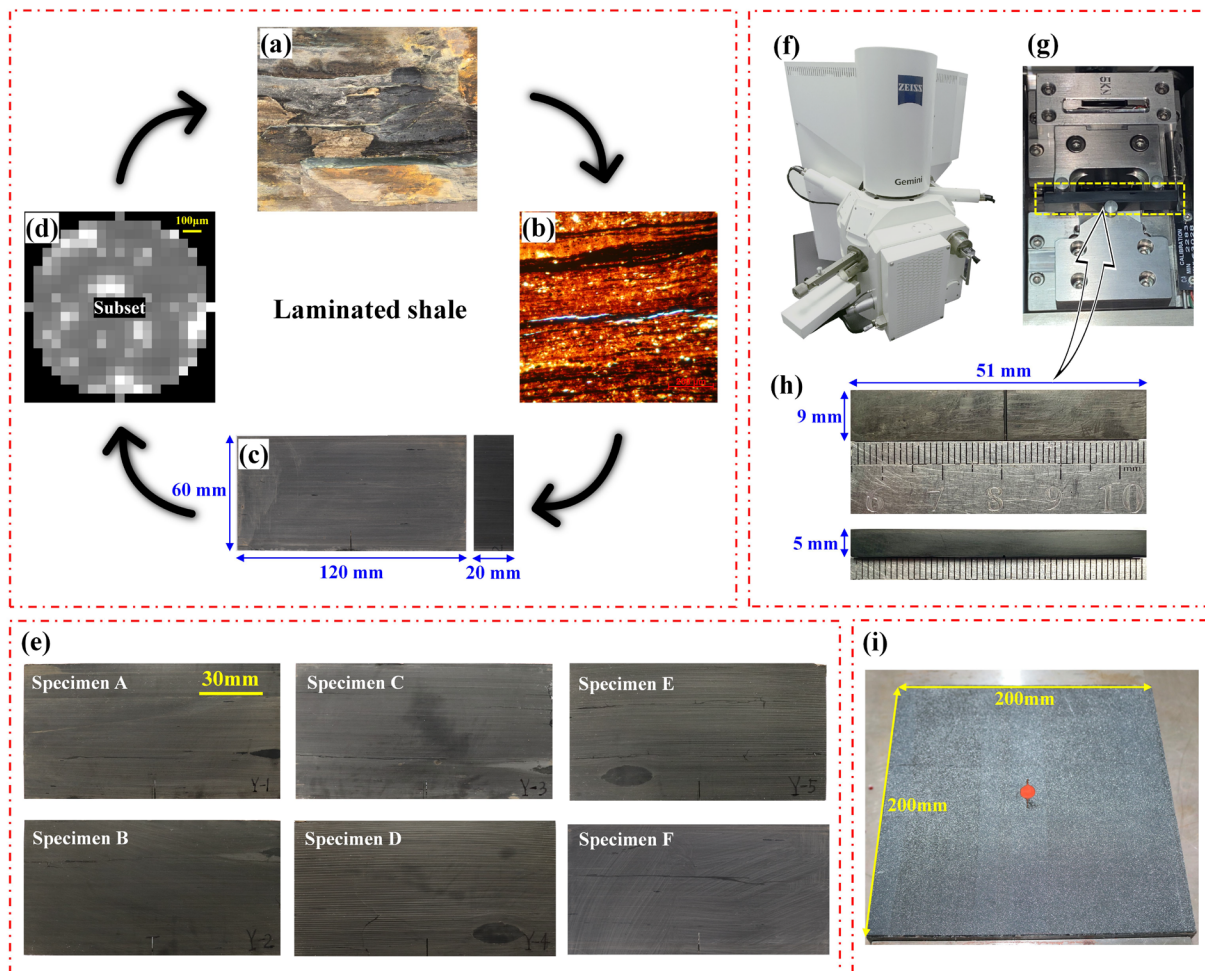


Fig. 1 Descriptions of the laminated shale. **a** Outcrop of Shaanxi shale; **b** micrographs of the casting thin section; **c** centimeter-scale shale specimen; **d** speckle of DIC and subset size; **e** specimens of

macro three-point bending tests; **f** sigma 500 FE-SEM system; **g** in situ loading system; **h** specimen of micro three-point bending test; **i** shale specimen of visual hydraulic fracturing experiment

Table 1 The size of the laminated shale specimens of Macro-TPB tests

Serial number	Length/mm	Height/mm	Thickness/mm	Prefabricated crack length/mm
Specimen A	119.90	63.53	20.71	9.43
Specimen B	119.91	63.73	20.50	9.68
Specimen C	120.33	64.07	20.59	9.41
Specimen D	120.16	64.75	23.85	10.12
Specimen E	120.01	64.50	19.82	9.49
Specimen F	119.56	60.55	20.12	10.50

opening displacement of the notch (COD) during Macro-TPB test, and the loading rate of COD was mainly set around 0.01 mm/min. The sizes of the specimens used in Macro-TPB experiments are listed in Table 1 and Fig. 1e.

For investigation of the micro-scale slip during fracture propagation, the field emission scanning electron microscope (FE-SEM) with an in situ loading system (Zhang et al. 2021) (Fig. 1f–g) was used to conduct micro three-point bending (Micro-TPB) experiment on the millimeter-scale shale. The FE-SEM is mainly composed of the electron optics system, signal detection system, vacuum system and computer, which uses the field emission electron gun to generate electron beams and stimulate electronic signals on the surface of rock samples. After the processing of detectors and computers, these signals could be converted into electronic images. In our experiment, the millimeter-scale specimen (shown in Fig. 1h) was loaded by the in situ loading system, while the electronic photograph was obtained by FE-SEM every 5 N loading. Considering the weak mechanical properties of interfaces, all the shale specimens used in this paper were processed by wire cutting to decrease the damage.

To study the interlaminar slip nucleation during hydraulic fracture propagation, the visual hydraulic fracturing (VHF) experiment was conducted on the decimeter-scale shale specimen using the designed equipment (Chen et al. 2019). This equipment is mainly used to conduct hydraulic fracturing experiments on two-dimensional platelike specimens. In this paper, the specimen size of the marine laminated shale is 200mm × 200mm × 50mm, as in Fig. 1i, and the far-field stresses could be applied to the specimen by flat jacks. Compared with traditional hydraulic fracturing of three-dimensional specimens, the critical advantage of VHF is capable of observing the initiation and propagation of hydraulic fractures through the transparent acrylic window. The experimental system of VHF mainly consists of a loading device, a constant rate injection pump, pressure sensors, and a digital camera. The black and white speckles are sprayed on the specimen surface for monitoring the displacements using digital imaging during fracturing.

2.2 Monitoring Methods

When studying the deformation of interlaminations, it is critical to measure the displacement of specimens during loading. As a non-contact optical detection method for monitoring the deformation, the digital image correlation method (DIC) has been widely used in the research of rock fracture mechanics (Chen et al. 2019; Pan et al. 2021; Xing et al. 2020). The significant advantage of DIC lies in its ability to depict the full-field deformation and obtain continuous information with high accuracy (Xing et al. 2020). The displacement changes are calculated according to the correlation of subsets before and after deformation, where the subset is a pixel value matrix (Xing et al. 2020). As shown in Eq. (1) (Blaber et al. 2015; Xing et al. 2020), the normalized cross-correlation criterion is adopted to track the subsets, and the open-source package proposed by Blaber et al. was used for obtaining the displacements and strains in this paper (Blaber et al. 2015). Figure 1d shows the image of speckle quality and subset size of Macro-TPB specimens.

$$\gamma = \frac{\sum_{(i,j) \in S} (f(\tilde{x}_{refi}, \tilde{y}_{refi}) - f_m)(g(\tilde{x}_{curi}, \tilde{y}_{curi}) - g_m)}{\sqrt{\sum_{(i,j) \in S} [f(\tilde{x}_{refi}, \tilde{y}_{refi}) - f_m]^2 \sum_{(i,j) \in S} [g(\tilde{x}_{curi}, \tilde{y}_{curi}) - g_m]^2}}, \quad (1)$$

where γ is the correlation coefficient of subset before and after deformation, S is the calculated area in correlation criterion, $(\tilde{x}_{refi}, \tilde{y}_{refi})$ and $(\tilde{x}_{curi}, \tilde{y}_{curi})$ are the local coordinates in the reference and current images, f and g are the grayscale intensity functions at position (x, y) in the reference and current images, and functions f_m and g_m refer to the average gray values of the reference and current subsets.

2.3 Typical Results of the Macro-TPB Experiment

The typical Macro-TPB results of laminated shale specimens are shown in Fig. 2, where Fig. 2a, b show the loading curves. Figure 2c, d show the horizontal (x -direction) displacement field after fracture propagation, which present stepped characteristics because of the effect of weak interfaces. Unlike the fracture propagation in homogeneous rocks, fracture in laminated shale tends to reorient at the weak interface. With loading, the fracture first extends along the direction of the prefabricated crack, and the propagation direction may change along the weak interface. Due to the high brittleness and interlamination development of shale, the loading curves in this paper are different from those in conventional experiments, with the characteristics of discontinuous decline.

The decrease of loading indicates the further propagation or slippage of fractures. Specifically, the slow rise of loading stress means the quasi-static development of the fractures, while the sudden drop of stress indicates the fast propagation of the fracture. Taking Specimen A as an example, when the COD is close to 93 μm , the stress decreases and the slipping fracture forms. However, we find that the interlaminar deformation has already occurred before the stress drop, meaning that the slip nucleation zone is generated before the formation of a full slipping fracture.

3 Identification of the Slip Nucleation Zone from Digital Imaging

3.1 Description Model of SNZ

SNZ is the development zone before the formation of a cohesionless slip (Azad et al. 2017; Uenishi and Rice 2003), generally characterized by the slip weakening model in theory (Chen and Knopoff 1986; Garagash and Germanovich 2012; Kato 2012; Uenishi and Rice 2003). Figure 3a shows the schematic diagram of the slip nucleation zone ahead of an opening-mode fracture. When a weak interface exists ahead of the tensile fracture, if the shear stress is greater than the static friction of interlamination, SNZ will be generated along the bedding plane. In the slip weakening model, the slip displacement is zero at the end of the SNZ, and the slip displacement is the largest at the beginning. Friction force exists at the interlaminar surface, resulting in a negative stress intensity factor. Thus, the positive stress intensity factor generated by external stress would be counteracted, to avoid the singularity of the fracture tip (Chen and Knopoff 1986; Rice 1979).

The linear slip weakening model (LSWM) is a common model for characterizing the constitutive relation of SNZ (Chen & Knopoff 1986; Knopoff et al. 2000), which is

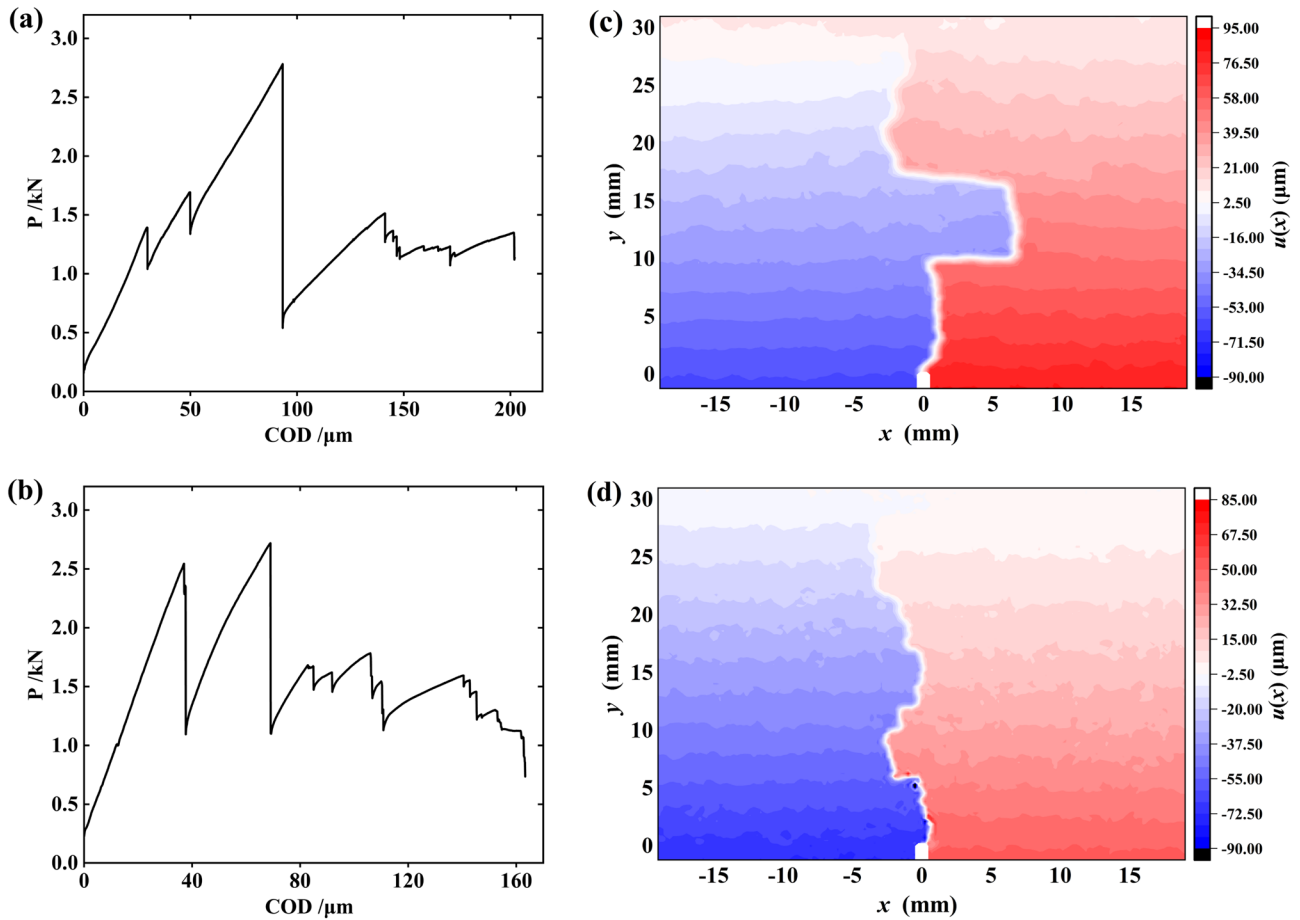


Fig. 2 Typical loading curves and horizontal displacement field monitored by DIC. **a** Loading curve of Specimen A; **b** loading curve of Specimen B; **c** horizontal displacement contours of Specimen A; **d** horizontal displacement contours of Specimen B

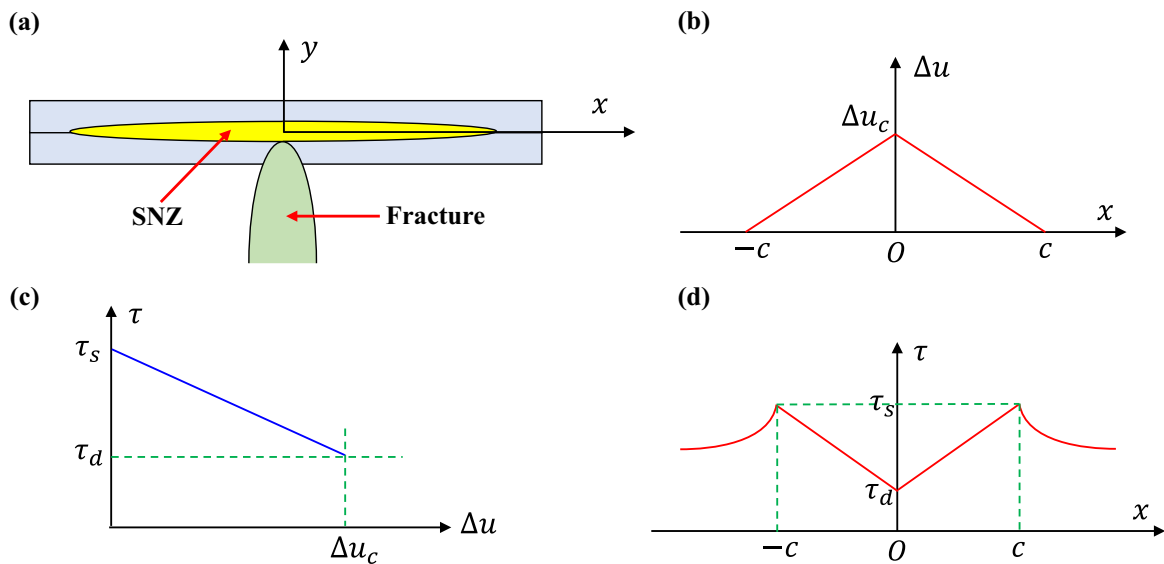


Fig. 3 Schematic diagram of slip nucleation zone and linear slip weakening model. **a** Slip nucleation zone induced by a vertical tensile fracture; **b** distribution of slip displacements in x -direction; **c** relation of shear stress and slip displacement; **d** stress distribution in x -direction

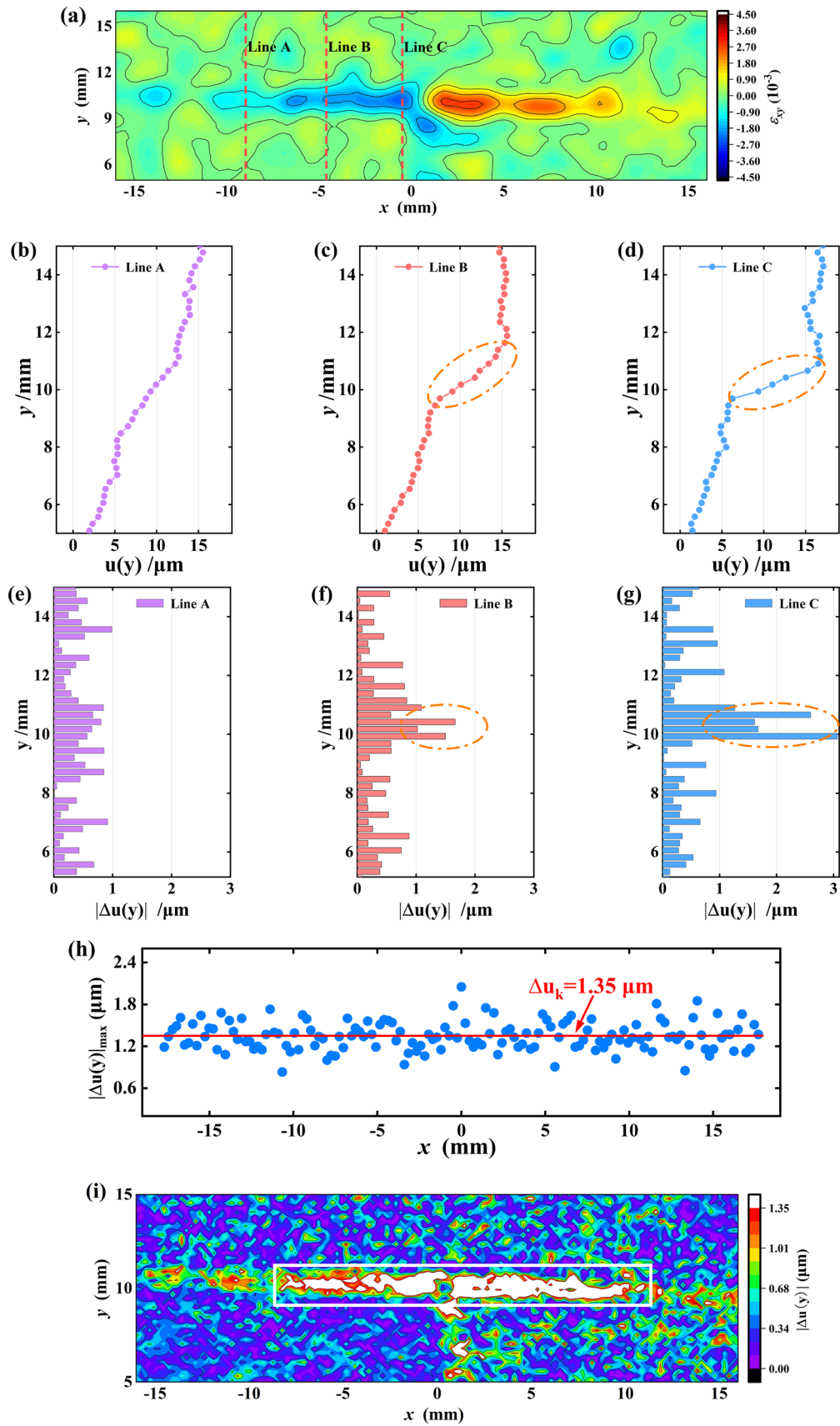


Fig. 4 SNZ characterization at 78% of peak load of Specimen A. **a** Contours of shear strain; **b** $u(y)$ distribution at Line A; **c** $u(y)$ distribution at Line B; **d** $u(y)$ distribution at Line C; **e** distribution of $|\Delta u(y)|$ at Line A; **f** distribution of $|\Delta u(y)|$ at Line B; **g** distribution of $|\Delta u(y)|$ at Line C; **h** distribution of $|\Delta u(y)|_{\max}$ in x -direction; **i** identification of SNZ based on the contours of $|\Delta u(y)|$

related to the static friction force (τ_s), kinetic friction force (τ_d) and critical slip displacement (Δu_c) (Eq. (2)), as shown in Fig. 3(c). In the linear slip weakening model, the slip displacement is Δu_c and the interlaminar shear stress is equal to τ_d at the beginning of SNZ ($x = 0$). At the end of the SNZ ($|x| = c$), Δu is zero and the shear stress is τ_s , as shown in Fig. 3b, d. The constitutive relation of SNZ along x -direction is shown in Eq. (3) (Chen and Knopoff 1986).

In the cohesive zone model of Mode-I fracture, the fracture process zone was characterized as a cohesive fracture. In fact, the slip weakening model is the generalization of the cohesive zone model in Mode-II fracture (Rice 1979), so SNZ could also be understood as a cohesive slip for the similar effects of cohesions during fracture development. The significant feature of cohesive slip is that the interlaminar shear stress would vary with the slip displacements. The cohesionless slip could be divided into cohesionless slipping and cohesionless slipped fracture. If we consider the full process of interlaminar slip during fracture propagation, three parts can be summarized: 1) slip nucleation zone (cohesive slip): $0 < \Delta u < \Delta u_c$, and τ will change with Δu ; 2) cohesionless slipping fracture: $\Delta u > \Delta u_c$, and τ is equal to τ_d , keeping constant; 3) cohesionless slipped fracture: Δu does not increase, and slip stops at this stage.

$$\tau = \tau_s - (\tau_s - \tau_d) \frac{\Delta u}{\Delta u_c}, \tag{2}$$

$$\tau(x) = \tau_s - (\tau_s - \tau_d) \frac{c-x}{c}, \tag{3}$$

where τ is the shear stress, τ_s static friction force, τ_d kinetic friction force, Δu slip displacement, Δu_c critical slip displacement, and c the position where $\tau = \tau_s$.

3.2 Identification of SNZ Using DIC

Although the linear slip weakening model has been used in the study of SNZ (Chen and Knopoff 1986; Knopoff et al. 2000), the relevant research lacked experimental verifications using digital imaging. DIC has been widely used to monitor the Mode-I fracture development process (Gao et al. 2022; Li and Einstein 2017; Lin et al. 2020; Pan et al. 2021), but how to use DIC to identify the slip nucleation zone remains to be studied at present.

Based on LSWM, a linear variation of the slip displacement exists in the slip nucleation zone on both sides of

the vertical tensile fracture tip. When the vertical measurement lines were selected to monitor the variation of horizontal displacements in the y -direction, significant discontinuities could be found from the displacement curves, where the discontinuity difference Δu is the slip displacement, decreasing from $x = 0$ to $x = c$. In this paper, $u(y)$ was used to investigate the interlaminar slip in the x -direction, while $u(x)$ was mainly used to detect the opening of the Mode-I fracture in the y -direction.

Different from the strain concentration of ϵ_{xx} in the Mode-I fracture process zone, slip displacement Δu would be generated in slip nucleation zone, leading to the concentration of ϵ_{xy} . As shown in Fig. 4a, ϵ_{xy} concentrates at the weak interface because of the inducement of the tensile fracture. Three vertical monitoring lines (A/B/C) are selected in Fig. 4a, and the corresponding displacement curves $u(y)$ are shown in Fig. 4b–d, where an obvious discontinuity with large slip displacement is found at Line C. Nonlinear characteristics still exist at Line B, but the discontinuous feature of horizontal displacement disappears at Line A. The distribution characteristics of $u(y)$ can provide a basis for judging the generation of SNZ. However, due to the objective error of DIC, it is impossible to define the accurate position where the slip displacement is zero. Therefore, the size of SNZ is difficult to be identified by $u(y)$ curves intuitively.

To identify SNZ accurately, the absolute value $|\Delta u(y)|$ between the adjacent monitoring points of $u(y)$ is introduced to characterize SNZ. As shown in Fig. 4f, g, $|\Delta u(y)|$ in the slip nucleation zone is higher than those in the elastic zone. At the end of SNZ, the distribution of $|\Delta u(y)|$ at the weak interface approximates to the elastic zone (Fig. 4e). In the linear slip weakening model, the area where $|\Delta u(y)| > 0$ is defined as SNZ. However, the objective error of DIC monitoring decides that $|\Delta u(y)|$ won't be equal to zero, so a threshold Δu_k needs to be defined. That is, SNZ is considered formed when $|\Delta u(y)| > \Delta u_k$. Δu_k is associated with the monitoring error of DIC. As $|\Delta u(y)|$ in SNZ is significantly higher than that in the elastic zone, it is reasonable to set Δu_k as the maximum of $|\Delta u(y)|$ in the elastic zone. In this paper, we determine Δu_k by the average of $|\Delta u(y)|_{\max}$ in different positions of the elastic zone. Taking Specimen A as an example, the horizontal distributions of $|\Delta u(y)|_{\max}$ in the elastic zone are shown in Fig. 4h, where $\Delta u_k = 1.35\mu\text{m}$.

The definition of thresholds Δu_k provides a standard to determine the length of SNZ. In this paper, we characterize SNZ by the contours of $|\Delta u(y)|$, of which the development scale and morphology could be identified intuitively. As in Fig. 4i, when the calibration of the contours is limited in $(0 - \Delta u_k)$, the white zone where $|\Delta u(y)| > \Delta u_k$ is the slip nucleation zone.

4 The Development Characteristics of the Slip Nucleation Zone

4.1 Development of SNZ During the Opening of Tensile Fracture

Based on LSWM, this paper proposed a method to identify the slip nucleation zone using DIC, showing the quasi-static development of SNZ before the formation of a cohesionless slip.

Figure 5a–d presents the development process of slip nucleation in Specimen A when the vertical tensile fracture length is 9.69 mm (referring to the y-axis of Fig. 5). The development maturity of SNZ varies in the horizontal direction: SNZ is more developed when the position is closer to the tip of the tensile fracture (around $x = 0$ mm), and the development of SNZ becomes less obvious far from the tip, consistent with the linear slip weakening model.

Before the cohesionless slipping of interlamination, the development lengths of SNZ (l_s) on both sides of the tensile fracture tip increased with loading stress (Fig. 5a–d). According to previous studies (Uenishi and Rice 2003), l_s of Mode-II slipping fracture depends on the shear modulus G , Poisson's ratio ν and slip weakening rate R , as shown in Eq. (4) (Uenishi and Rice 2003). In the linear slip weakening model, $R = (\tau_s - \tau_d) / \Delta u_c$, thus l_s can be characterized by Eq. (5).

$$l_s = \alpha \frac{GR}{1-\nu}, \quad (4)$$

$$l_s = \alpha \frac{G\Delta u_c}{(1-\nu)(\tau_s - \tau_d)}, \quad (5)$$

where G is shear modulus, ν Poisson's ratio, R slip weakening rate, and α is a fixed constant.

According to Eq. (5), a key parameter related to l_s is the critical slip displacement Δu_c . To study the induced effect of Mode-I fracture on Δu_c , the fracture tip opening displacements (Lin et al. 2014, 2020) under different loading stress were characterized when the fracture propagates to the weak interface, as shown in Fig. 6a. The critical slip displacement of SNZ presents a positive linear correlation with the Mode-I fracture tip opening displacement (Fig. 6b), as shown in Eq. (6). In the three-point bending experiments, the normal stress of interlamination increases with loading stress, so the change of interlaminar friction force should be considered. The experimental results show a linear correlation between the loading stress P and the fracture tip opening displacements w (Eq. (7)). In Specimen A, the values of the linear fitting parameters (a , b , c and d) are 0.60, 1.78, 0.10 and 0.24, respectively. Combining Eqs. (4)–(7), we can obtain the formula (Eq. (8)) of SNZ length induced by a vertical tensile fracture in the three-point bending experiment, i.e., l_s is characterized by the fracture tip opening displacements. During the slip nucleation, l_s increases nonlinearly with w (Fig. 6c), consistent with the results obtained by DIC (Fig. 5a–d). The characterization of interlaminar fracture energy G_s and slip weakening rate R considering w are shown in Eq. (9, 10), where G_s increases quadratically and R decreases nonlinearly with the increase of w (Fig. 6d).

$$\Delta u_c = a \cdot w - b, \quad (6)$$

$$P = c \cdot w + d, \quad (7)$$

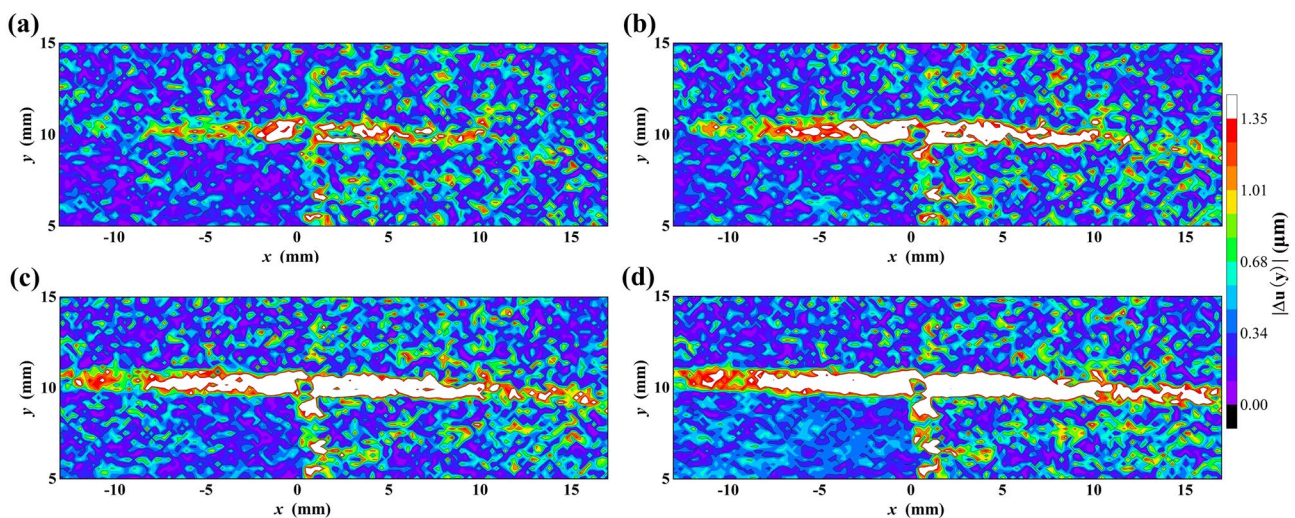


Fig. 5 Development characteristics of SNZ under different loading stress (Specimen A). **a** 55.75% pre-peak; **b** 70.50% pre-peak; **c** 84.89% pre-peak; **d** the peak

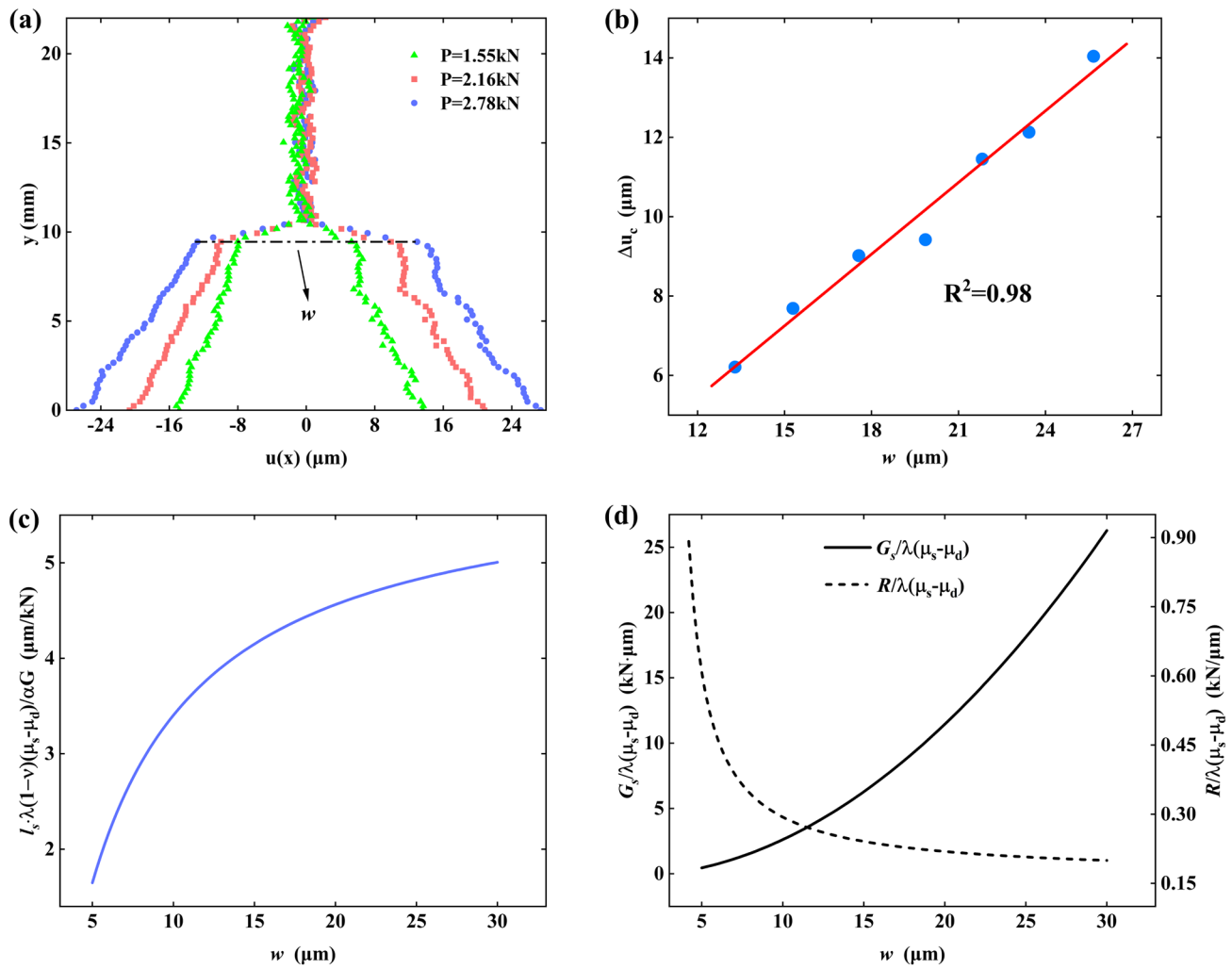


Fig. 6 Description of the fracture tip opening displacement (Specimen A). **a** Identification of the fracture tip opening displacements; **b** the relationship between w and Δu_c ; **c** change of l_s influenced by w ; **d** change of G_s and R influenced by w

$$l_s = \alpha \frac{G(a \cdot w - b)}{\lambda(1-\nu)(\mu_s - \mu_d)(c \cdot w + d)}, \tag{8}$$

$$G_s = \lambda(\mu_s - \mu_d)(c \cdot w + d)(a \cdot w - b)/2, \tag{9}$$

$$R = \frac{\lambda(\mu_s - \mu_d)(c \cdot w + d)}{(a \cdot w - b)}, \tag{10}$$

where a and b are the linear fitting parameters of w and Δu_c , c, d the linear fitting parameters of w and P , w the fracture tip opening displacement, G_s the interlaminar slipping fracture energy, λ the conversion coefficient between loading load and interlaminar stress, μ_s the coefficient of static friction, and μ_d the coefficient of kinetic friction.

4.2 Formation of the Cohesionless Slipping Fracture from an SNZ

From the cohesive zone model of Mode-I fracture and the slip weakening model, when the vertical fracture arrives at the weak interface, the development process will be transformed from FPZ to SNZ if the interlaminar shear stress reaches the static friction (τ_s), and the increased energy mainly dissipates in the slip nucleation.

The appearance of SNZ indicates the formation of a slipping fracture. As shown in Fig. 5a–d and Fig. 7d–f, the generation of SNZ always presents in pairs, with asymmetric distributions, mainly due to the inhomogeneous distribution of interlaminar mechanical properties.

Figure 7a–c shows that the slipping fractures always propagate along the side with a longer SNZ after nucleation. The difference in length between the conjugated SNZs

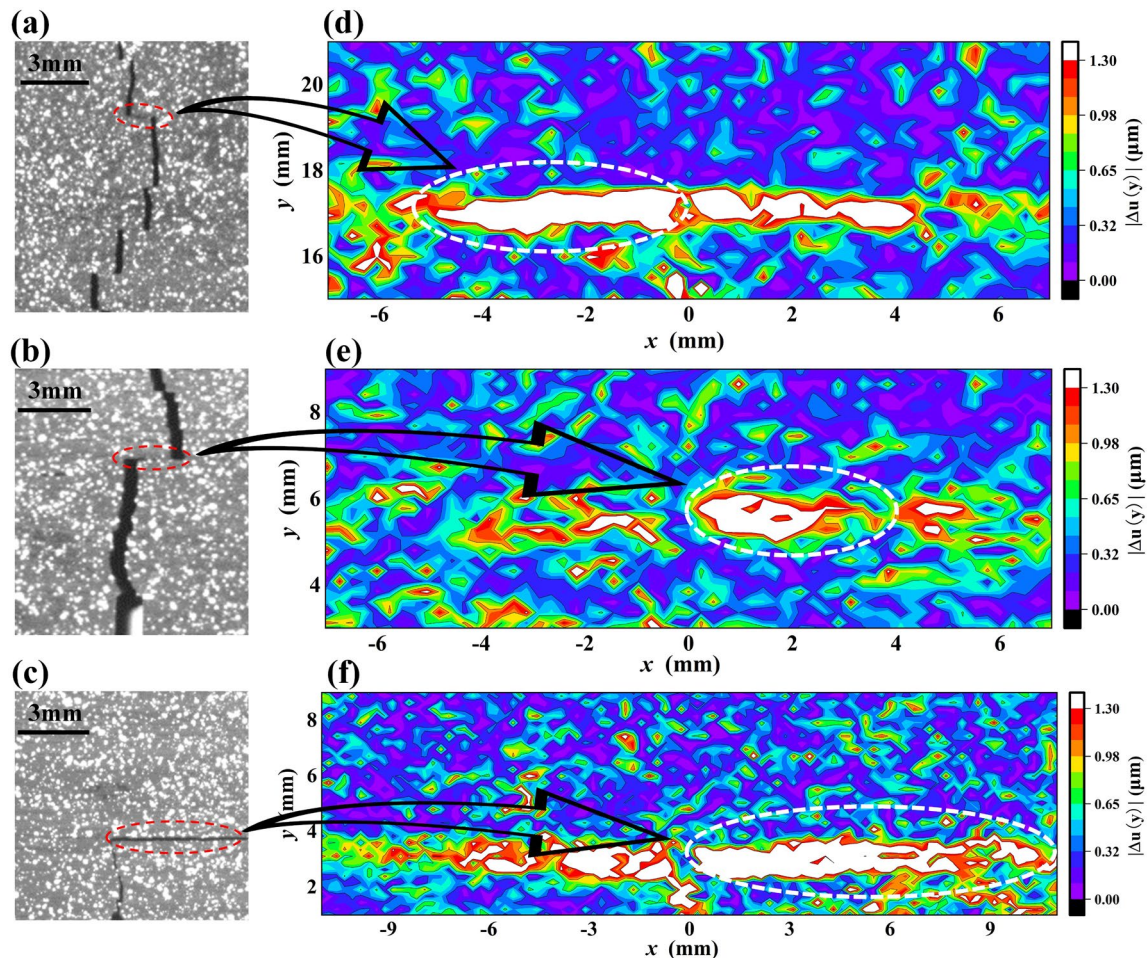


Fig. 7 Fracture slip path and SNZ contour plot. **a** Fracture propagation path of Specimen B; **b** fracture propagation path of Specimen C; **c** fracture propagation path of Specimen D; **d** SNZ of Specimen B

when the tensile fracture length is 16.95 mm; **e** SNZ of Specimen C when the tensile fracture length is 5.28 mm; **f** SNZ of Specimen D when the tensile fracture length is 2.64 mm

determines the propagation direction of subsequent cohesionless slipping: the cohesionless slipping occurs in the direction with a larger SNZ length. Since the critical slip displacements Δu_c of the conjugated SNZs are the same at the beginning ($x = 0$), the main factor affecting the development size of SNZ is the interlaminar mechanical properties referring to the calculation formula of SNZ length (Eq. (5)). In this paper, the slip nucleation factor Ω is defined as shown in Eq. (11), which is used to compare the mechanical properties of conjugated SNZs and judge the propagation direction of slip. In the conjugated SNZs, the cohesionless slips prefer to develop along the side with a larger Ω . Thus, the difference between kinetic and static frictions will be the decisive factor when the parameters G and ν are the same.

$$\Omega = \frac{G}{(1-\nu)(\tau_s - \tau_d)}, \quad (11)$$

where Ω is the slip nucleation factor.

4.3 Slip Nucleation of Millimeter-Scale Specimen Scanned by an Electron Microscope

Based on the Macro-TPB results, the slip nucleation and the formation of cohesionless slips during opening-mode fracturing have been studied on centimeter-scale specimens. To study the micro-scale slip nucleation, we adopted a real-time electron microscope to detect the fracture propagation of the millimeter-scale specimen in the Micro-TPB experiment.

Figure 8c shows the microscopic characteristics of Shaanxi laminated shale with 200 times magnification,

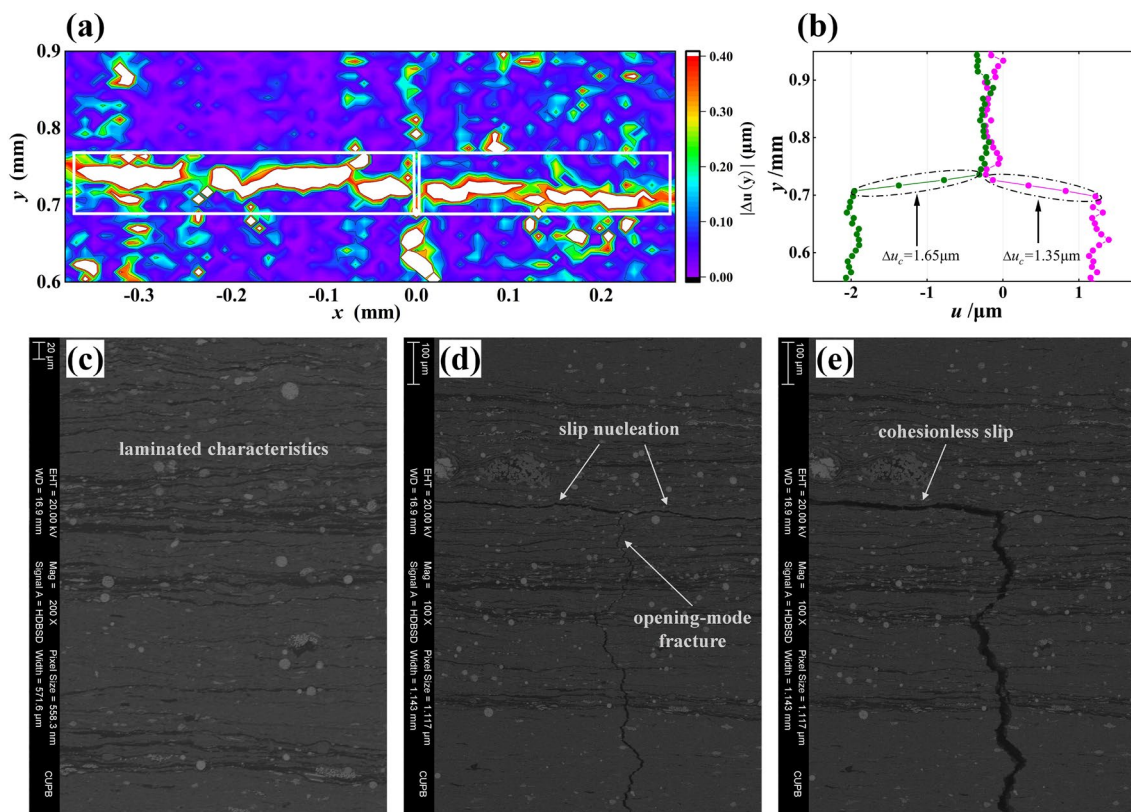


Fig. 8 Results of micro-scale fracture experiment. **a** Digital imaging of slip nucleation; **b** critical slip displacements; **c** electron microscope photos with 200 × magnification; **d** electron microscope photos with

100 × magnification: slip nucleation; **e** electron microscope photos with 100 × magnification: cohesionless slip

where the laminated distributions are more obvious. DIC analysis was carried out on the electron microscope photos with 100 times magnification (Fig. 8a). We found that when the micro-scale opening fracture propagated to the weak interface (Fig. 8d), a pair of conjugated SNZs appeared at the interlamination, as shown by the digital imaging in Fig. 8a. Compared with the Macro-TPB results, the length of SNZ on the micro-scale is only hundreds of micrometers, and the critical slip displacements on the left/right sides of the tensile fracture tip are only 1.65 μm/1.35 μm (Fig. 8b), which is about an order of magnitude smaller than the Macro-TPB results.

Consistent with the Macro-TPB fracture experimental results, the SNZs observed in the Micro-TPB test present asymmetric developments (Fig. 8a), and the side with a longer SNZ is accompanied by a larger critical slip displacement, following the prediction of Eq. (5). Finally, the cohesionless slipping fracture propagated along the side with a longer SNZ, as shown in Fig. 8e. In summary, the development of SNZ and the formation of cohesionless slipping show similarities at the different scales of shale.

5 Discussion of the Fracture Nucleation During Hydraulic Fracturing in Laminated Shale

5.1 An Experimental Validation from the Visual Hydraulic Fracturing

In the laboratory, the three-point bending test is a common method (Lin et al. 2020; Pan et al. 2021; Xing et al. 2019; Zhang et al. 2018) used to study the mechanical behaviors of hydraulic fractures. Based on the fracture results of laminated shale, we found the conjugated SNZs would be generated before fracture reorientation, and the cohesionless slip will appear on the side with a more developed SNZ. However, whether the development characteristics of the SNZ during hydraulic fracturing are consistent with the three-point bending experiments needs further validation. Therefore, using DIC to monitor the propagation of hydraulic fractures (AlTammar et al. 2019; Li and Einstein

2019) will help to verify the conclusions, especially in laminated shale.

To study the slip nucleation during hydraulic fracture propagation, the visual hydraulic fracturing experiment was carried out on the shale specimen. Unlike in the three-point bending test, the shale specimen was applied with a constant stress perpendicular to the lamination, approximately 3 MPa, and the pressure fluid composed of water, guar gum, and red dye was injected. During the fracturing process, we found that a pair of asymmetrical slip nucleation zones also appeared when the hydraulic fracture propagated to the weak interface (Fig. 9c). With the increase of w , the development size of SNZ also increased (Fig. 9b), and the cohesionless slipping fracture was finally generated on the side with a larger SNZ (Fig. 9(d)). According to Eqs. (5), (6), in hydraulic fracturing, l_s linearly increases with w , which is consistent with our monitoring results (Fig. 9b), indicating that the linear slip weakening model is reasonable for characterizing the quasi-static nucleation process.

Figure 9(a) shows the experimental results of visual hydraulic fracturing in decimeter-scale shale, where the hydraulic fracture propagates from the vertical direction to the weak interface, as predicted by the longer SNZ. The analyses above indicate that the conclusions about the slip nucleation obtained by three-point bending experiments are suitable for discussing hydraulic fracturing in shale formations. In addition, the slip nucleation and cohesionless slip of laminated shale show similarities at different scales from millimeter, centimeter to decimeter.

5.2 The Residual Slip Zone After the Fracture Propagation

The conjugated slip nucleation zones would appear before the fracture propagates along the interlaminations. However, how the shorter SNZ will change after fracture propagation is still unclear. In this paper, the residual slip zone (RSZ) is defined as the side with an initial SNZ, but without forming a cohesionless slip during hydraulic fracturing.

To determine whether slippage exists in RSZ, the horizontal displacement curves perpendicular to RSZ were studied. Figure 10a–d presents the displacement distribution near RSZ in different positions, when the fracture opening displacement is 44.34 μm and the corresponding vertical tensile fracture length is 11.89 mm. Significant discontinuities were observed in the horizontal displacement, indicating that slippage still exists in RSZ after fracture propagation. Figure 10a–d shows that the slippage becomes smaller at a farther distance from the fracture turning point, indicating that the slip nucleation is still retained in RSZ.

Since the initial SNZ size of the residual slip zone is smaller, it does not become the dominant path of cohesionless slip. However, when evaluating the hydraulic fracture system, not only macroscopic fractures but also the potential fractures represented by RSZ need to be studied. We found that slippage exists in RSZ. Therefore, RSZ also possesses hydraulic conductivity (Zhao et al. 2013) and should be regarded as a part of fracturing fractures of shale.

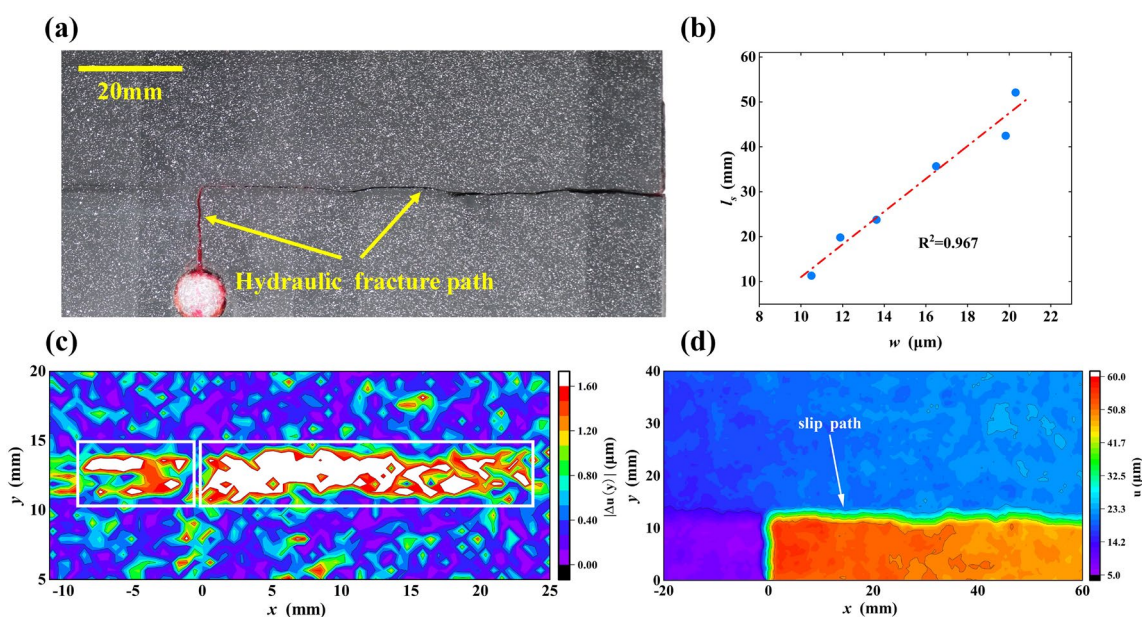


Fig. 9 Experimental results of the visual hydraulic fracturing in laminated shale. **a** Hydraulic fracture propagation path; **b** relationship between w and length of the longer SNZ; **c** SNZ when w is 13.63 μm ; **d** horizontal displacement contours when w is 35.94 μm

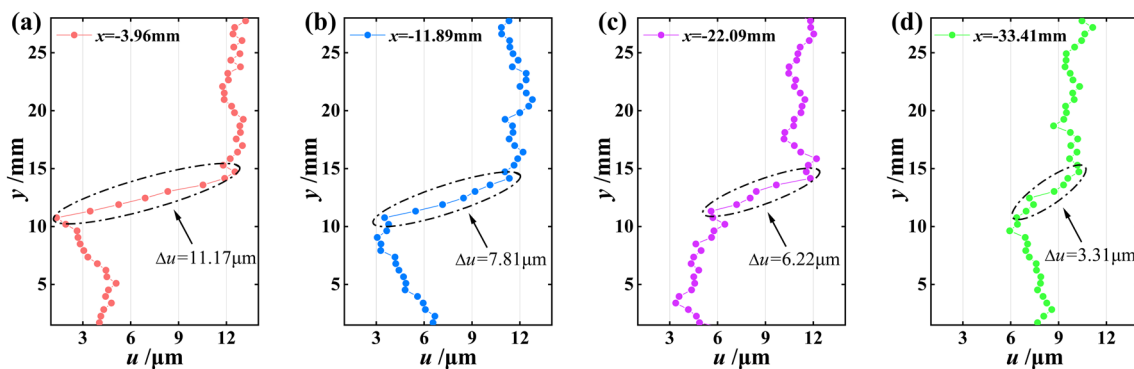


Fig. 10 Slippage in RSZ after fracture propagation (specimen of the visual hydraulic fracturing). **a** $x = -3.96$ mm; **b** $x = -11.89$ mm; **c** $x = -22.09$ mm; **d** $x = -33.41$ mm

5.3 Fracture Nucleation Modes During Hydraulic Fracturing

Hydraulic fracturing is an effective technique in the stimulation of shale oil reservoirs. The findings in this paper help to understand the slip nucleation behavior during hydraulic fracturing. However, the nucleation mode of hydraulic

fractures in laminated shale still needs to be discussed based on the research in this paper and previous related works (AITammar et al. 2019; Chen et al. 2021; Pan et al. 2021; Yao 2012).

The nonlinear development of hydraulic fractures in layered shale formations could be divided into two modes: one is the development of fracture process zone when the fracture propagates vertically, and the other is the development of slip

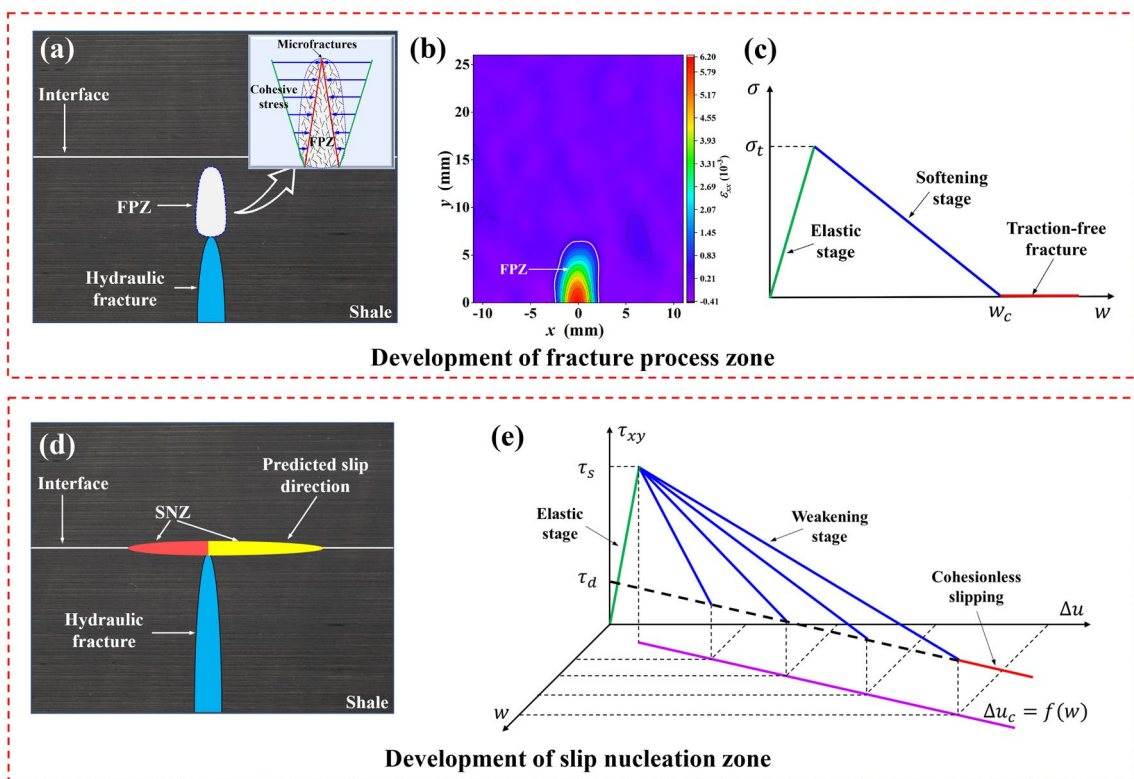


Fig. 11 Development characteristics of hydraulic fractures in laminated shale. **a** Diagram of FPZ development; **b** FPZ ahead of the pre-fabricated fracture in Specimen C; **c** constitutive relationship of FPZ;

d diagram of SNZ ahead of a hydraulic fracture; **e** LSWM considering the fracture tip opening displacements

nucleation zone when the fracture slips at the interlamination. As shown in Fig. 11a, when the hydraulic fracture propagates vertically without reaching the weak interface, the fracture process zone (FPZ) will be developed in front of the fracture tip, presenting microfractures aggregation (Fig. 11a) as well as tensile stress softening (Fig. 11c) (Chen et al. 2021; Elices et al. 2001; Lin et al. 2020). It is common to describe the fracture process zone as a cohesive tensile fracture based on the cohesive zone model (Q. Lin et al. 2020), and the tensile stress ahead of hydraulic fracture will begin to soften when the rocks reach the tensile strength. The corresponding constitutive model is illustrated in Eq. (12), which characterizes the relationship between tensile stress and fracture opening displacements. Combining with the existing FPZ identification method (Chen et al. 2021), the FPZ shape can be characterized based on DIC, as in Fig. 11(b).

$$\sigma = f(w), \quad (12)$$

where σ is the tensile stress.

The fully developed fracture process zone means the formation of a new fracture, and the vertical fracture will propagate forward. When the vertical fracture propagates near the weak interface, the interlaminar elastic deformation will occur first (Fig. 11e). When the interlaminar shear stress reaches the static friction force, the interface becomes weakening, accompanied by the generation of SNZ. Due to the inhomogeneous distribution of interlaminar mechanical properties (different values of Ω), SNZs will present an asymmetric distribution (Fig. 11d). After the quasi-static slip nucleation, a cohesionless slip would be formed along the side with a longer SNZ. The linear slip weakening model considering the fracture tip opening displacements is shown in Fig. 11e (Chen and Knopoff 1986; Rice 1979). With the increase of hydraulic fracture tip opening displacement, the development length of SNZ l_s and interlaminar fracture energy G_f increase, but the slip weakening rate R decreases.

When the opening displacements of the hydraulic fracture tip increase to a certain value, the cohesionless slip will be generated along the side with a longer SNZ (Ω is larger), while the other side will be transformed into a residual slip zone. RSZ was neglected in previous evaluations of hydraulic fracture systems. Although the formation of RSZ consumes fracture energy, slippage exists in RSZ. Therefore, RSZ should be the effective fracture with enhanced hydraulic conductivity, a part of the hydraulic fracture systems in shale formations.

6 Conclusions

In this paper, the laminated shale was used in the macro and micro three-point bending experiments, as well as the visual hydraulic fracturing experiment, where DIC was used to monitor the interlaminar deformation. The slip nucleation during fracture propagation was observed in the shale specimens from millimeter scale to decimeter scale. The findings could help to understand the generation process of interlaminar slip during hydraulic fracturing, summarized as follows:

1. Based on the linear slip weakening model, we proposed a method to identify the slip nucleation zone using DIC, visually detecting the SNZ size. Two asymmetric SNZs were observed on both sides of the tensile fracture tip before the formation of a cohesionless slip.
2. The cohesionless slipping direction could be predicted according to the development size of the conjugated SNZs, where the cohesionless slip will be generated along the side with a longer SNZ, as judged by the defined factor Ω . The side with a smaller difference value of kinetic and static friction force will be the preferred path of cohesionless slipping.
3. For SNZ development, the linear slip weakening model considering the fracture tip opening displacements was discussed. With the increase of w , SNZ length and interlaminar fracture energy will increase, whereas the slip weakening rate will decrease.
4. The results of visual hydraulic fracturing verified the applicability of slip nucleation in shale formations, where two nucleation modes (FPZ and SNZ) will be generated during fracturing. With the characteristics of slippage, the residual slip zone was defined, which should be a potential part of the hydraulic fracture systems.

Acknowledgements This work was financially supported by the National Natural Science Foundation of China (No. 51925405, No. 52174011 & No. 52104050) and the Strategic Cooperation Projects of CNPC and CUPB (ZLZX2020-02).

Author Contributions LC: conceptualization, methodology, writing—original draft. GZ: supervision, methodology, funding acquisition. MZ: investigation, validation. CZ: data curation, visualization. ZF: data curation. JZ: writing—review and editing, critical revision of the draft. DZ: writing—review and editing. SL: project administration, funding acquisition.

Data availability The data that support the findings of this study are available from the corresponding author upon reasonable request.

Declarations

Conflict of Interest The authors declare that they have no known competing financial interests or personal relationships that could have appeared to influence the work reported in this paper.

References

- AlTammar MJ, Agrawal S, Sharma MM (2019) Effect of geological layer properties on hydraulic-fracture initiation and propagation: an experimental study. *SPE J* 24(2):757–794. <https://doi.org/10.2118/184871-PA>
- Ampuero J-P, Vilotte J-P, Sánchez-Sesma FJ (2002) Nucleation of rupture under slip dependent friction law: Simple models of fault zone. *J Geophys Res* 107(12):2–19. <https://doi.org/10.1029/2001JB000452>
- Azad M, Garagash DI, Satish M (2017) Nucleation of dynamic slip on a hydraulically fractured fault. *J Geophys Res* 122(4):2812–2830. <https://doi.org/10.1002/2016JB013835>
- Barenblatt GI (1962) The mathematical theory of equilibrium cracks in brittle fracture. *Adv Appl Mech* 7:55–129
- Blaber J, Adair B, Antoniou A (2015) Ncorr: open-source 2d digital image correlation matlab software. *Exp Mech* 55(6):1105–1122. <https://doi.org/10.1007/s11340-015-0009-1>
- Chen YT, Knopoff L (1986) Static shear crack with a zone of slip-weakening. *Geophys J Roy Astron Soc* 87(3):1005–1024. <https://doi.org/10.1111/j.1365-246X.1986.tb01980.x>
- Chen L, Zhang G, Lyu Y, Li Z, Zheng X (2019) Visualization study of hydraulic fracture propagation in unconsolidated sandstones. In: 53rd US rock mechanics/geomechanics symposium. OnePetro, New York
- Chen L, Zhang G, Zou Z, Guo Y, Du X (2020) Experimental observation of fracture process zone in sandstone from digital imaging. In: 54th US rock mechanics/geomechanics symposium. OnePetro, Colorado
- Chen L, Zhang G, Zou Z, Guo Y, Zheng X (2021) The effect of fracture growth rate on fracture process zone development in quasi-brittle rock. *Eng Fract Mech* 258:108086. <https://doi.org/10.1016/j.engfracmech.2021.108086>
- Elices M, Guinea GV, Gómez J, Planas J (2001) The cohesive zone model: advantages, limitations and challenges. *Eng Fract Mech* 69(2):137–163. [https://doi.org/10.1016/S0013-7944\(01\)00083-2](https://doi.org/10.1016/S0013-7944(01)00083-2)
- Galybin AN, Mukhamediev SA (2014) Fracture development on a weak interface ahead of a fluid-driven crack. *Eng Fract Mech* 129:90–101. <https://doi.org/10.1016/j.engfracmech.2014.08.005>
- Gao Y, Dong Y, Chen L, Li Y, Qin J, Jiang Z (2022) An improved model for evaluating the brittleness of shale oil reservoirs based on dynamic elastic properties: a case study of lucaogou formation. *Jimusar Sag Geofluids* 2022:6711977. <https://doi.org/10.1155/2022/6711977>
- Garagash DI, Germanovich LN (2012) Nucleation and arrest of dynamic slip on a pressurized fault. *J Geophys Res* 117(10):1–27. <https://doi.org/10.1029/2012JB009209>
- Garcia X, Nagel N, Zhang F, Sanchez-Nagel M, Lee B (2013) Revisiting vertical hydraulic fracture propagation through layered formations—A numerical evaluation. In: 47th US rock mechanics/geomechanics symposium. OnePetro, California
- He J, Zhang Y, Li X, Wan X (2019) Experimental investigation on the fractures induced by hydraulic fracturing using freshwater and supercritical CO₂ in shale under uniaxial stress. *Rock Mech Rock Eng* 52(10):3585–3596. <https://doi.org/10.1007/s00603-019-01820-w>
- Hillerborg A, Modéer M, Petersson PE (1976) Analysis of crack formation and crack growth in concrete by means of fracture mechanics and finite elements. *Cem Concr Res* 6(6):773–781. [https://doi.org/10.1016/0008-8846\(76\)90007-7](https://doi.org/10.1016/0008-8846(76)90007-7)
- Hu S, Zhao W, Hou L, Yang Z, Zhu R, Wu S, Bai B, Jin X (2020) Development potential and technical strategy of continental shale oil in China. *Pet Explor Dev* 47(4):877–887. [https://doi.org/10.1016/S1876-3804\(20\)60103-3](https://doi.org/10.1016/S1876-3804(20)60103-3)
- Jia Y, Lu Z, Xiong Q, Hampton JC, Zhang Y, He P (2021) Laboratory characterization of cyclic hydraulic fracturing for deep shale application in Southwest China. *Int J Rock Mech Mining Sci* 148:104945. <https://doi.org/10.1016/j.ijrmms.2021.104945>
- Kato N (2012) Dependence of earthquake stress drop on critical slip-weakening distance. *J Geophys Res* 117(1):1–10. <https://doi.org/10.1029/2011JB008359>
- Knopoff L, Landoni JA, Abinante MS (2000) Causality constraint for fractures with linear slip weakening. *J Geophys Res* 105(B12):28035–28043. <https://doi.org/10.1029/2000JB900284>
- Li BQ, Einstein HH (2017) Comparison of visual and acoustic emission observations in a four point bending experiment on barre granite. *Rock Mech Rock Eng* 50(9):2277–2296. <https://doi.org/10.1007/s00603-017-1233-z>
- Li BQ, Einstein HH (2019) Direct and microseismic observations of hydraulic fracturing in barre granite and opalinus clayshale. *J Geophys Res* 124(11):11900–11916. <https://doi.org/10.1029/2019JB018376>
- Lin Q, Yuan H, Biolzi L, Labuz JF (2014) Opening and mixed mode fracture processes in a quasi-brittle material via digital imaging. *Eng Fract Mech* 131:176–193. <https://doi.org/10.1016/j.engfracmech.2014.07.028>
- Lin C, He J, Li X, Wan X, Zheng B (2017) An experimental investigation into the effects of the anisotropy of shale on hydraulic fracture propagation. *Rock Mech Rock Eng* 50(3):543–554. <https://doi.org/10.1007/s00603-016-1136-4>
- Lin Q, Wang S, Pan PZ, Bian X, Lu Y (2020) Imaging opening-mode fracture in sandstone under three-point bending: a direct identification of the fracture process zone and traction-free crack based on cohesive zone model. *Int J Rock Mech Mining Sci* 136:104516. <https://doi.org/10.1016/j.ijrmms.2020.104516>
- Min Z, Guangqing Z, Du X 2021 Characterization of Fracture Process in Shale: Insights from Micro-Scale DIC. 55th US Rock Mechanics/Geomechanics Symposium
- Nikolskiy D, Lecampion B (2020) Modeling of simultaneous propagation of multiple blade-like hydraulic fractures from a horizontal well. *Rock Mech Rock Eng* 53(4):1701–1718. <https://doi.org/10.1007/s00603-019-02002-4>
- Palmer AC, Rice JR, Hill R (1973) The growth of slip surfaces in the progressive failure of over-consolidated clay. *Proc Royal Soc London* 332(1591):527–548. <https://doi.org/10.1098/rspa.1973.0040>
- Pan R, Zhang G, Li S, Zheng X, Xu C, Fan Z (2021) Influence of the fracture process zone on fracture propagation mode in layered rocks. *J Petrol Sci Eng* 202:108524. <https://doi.org/10.1016/j.petrol.2021.108524>
- Renshaw CE, Pollard DD (1995) An experimentally verified criterion for propagation across unbounded frictional interfaces in brittle, linear elastic materials. *Int J Rock Mech Mining Sci* 32(3):237–249. [https://doi.org/10.1016/0148-9062\(94\)00037-4](https://doi.org/10.1016/0148-9062(94)00037-4)
- Rice JR (1979) The mechanics of earthquake rupture. In: Providence: division of engineering, vol 720. Brown University
- Saberhosseini SE, Ahangari K, Mohammadrezaei H (2019) Optimization of the horizontal-well multiple hydraulic fracturing operation in a low-permeability carbonate reservoir using fully coupled XFEM model. *Int J Rock Mech and Mining Sci* 114:33–45. <https://doi.org/10.1016/j.ijrmms.2018.09.007>

- Segall P, Pollard DP (1983) Nucleation and growth of strike slip faults in granite. *J Geophys Res* 88(B1):555–568. <https://doi.org/10.1029/JB088iB01p00555>
- Tan Y, Engelder T (2016) Further testing of the bedding-plane-slip model for hydraulic-fracture opening using moment-tensor inversions. *Geophysics* 81(5):159–168. <https://doi.org/10.1190/GEO2015-0370.1>
- Tan P, Jin Y, Han K, Hou B, Chen M, Guo X, Gao J (2017) Analysis of hydraulic fracture initiation and vertical propagation behavior in laminated shale formation. *Fuel* 206:482–493. <https://doi.org/10.1016/j.fuel.2017.05.033>
- Uenishi K, Rice JR (2003) Universal nucleation length for slip-weakening rupture instability under nonuniform fault loading. *J Geophys Res*. <https://doi.org/10.1029/2001JB001681>
- Warpinski NR, Teufel LW (1987) Influence of geologic discontinuities on hydraulic fracture propagation. *JPT J Pet Technol* 39(2):209–220. <https://doi.org/10.2118/13224-pa>
- Wu S, Gao K, Wang X, Ge H, Zou Y, Zhang X (2022) Investigating the propagation of multiple hydraulic fractures in shale oil rocks using acoustic emission. *Rock Mech Rock Eng*. <https://doi.org/10.1007/s00603-022-02960-2>
- Xing Y, Zhang G, Wan B, Zhao H (2019) Subcritical fracturing of sandstone characterized by the acoustic emission energy. *Rock Mech Rock Eng* 52(7):2459–2469. <https://doi.org/10.1007/s00603-018-1724-6>
- Xing Y, Huang B, Ning E, Zhao L, Jin F (2020) Quasi-static loading rate effects on fracture process zone development of mixed-mode (I-II) fractures in rock-like materials. *Eng Fract Mech*. <https://doi.org/10.1016/j.engfracmech.2020.107365>
- Yaghoubi A (2019) Hydraulic fracturing modeling using a discrete fracture network in the Barnett Shale. *Int J Rock Mech Min Sci* 119(January):98–108. <https://doi.org/10.1016/j.ijrmms.2019.01.015>
- Yan C, Deng J, Cheng Y, Li M, Feng Y, Li X (2017) Mechanical properties of gas shale during drilling operations. *Rock Mech Rock Eng* 50(7):1753–1765. <https://doi.org/10.1007/s00603-017-1203-5>
- Yao Y (2012) Linear elastic and cohesive fracture analysis to model hydraulic fracture in brittle and ductile rocks. *Rock Mech Rock Eng* 45(3):375–387. <https://doi.org/10.1007/s00603-011-0211-0>
- Zhang X, Jeffrey RG (2016) Fluid-driven nucleation and propagation of splay fractures from a permeable fault. *J Geophys Res* 121(7):5257–5277. <https://doi.org/10.1002/2015JB012546>
- Zhang G, Xing Y, Wang L (2018) Comprehensive sandstone fracturing characterization: integration of fiber Bragg grating, digital imaging correlation and acoustic emission measurements. *Eng Geol* 246(August):45–56. <https://doi.org/10.1016/j.enggeo.2018.09.016>
- Zhang F, Wang X, Tang M, Du X, Xu C, Tang J, Damjanac B (2021) Numerical investigation on hydraulic fracturing of extreme limited entry perforating in plug-and-perforation completion of shale oil reservoir in changqing oilfield. *China Rock Mech Rock Eng* 54(6):2925–2941. <https://doi.org/10.1007/s00603-021-02450-x>
- Zhao H, Chen H, Liu G, Li Y, Shi J, Ren P (2013) New insight into mechanisms of fracture network generation in shale gas reservoir. *J Petrol Sci Eng* 110:193–198. <https://doi.org/10.1016/j.petrol.2013.08.046>
- Zhao P, Gray KE (2021) Analytical and machine-learning analysis of hydraulic fracture-induced natural fracture slip. *SPE J*. <https://doi.org/10.2118/205346-pa>
- Zhou W, Shi G, Wang J, Liu J, Xu N, Liu P (2022) The influence of bedding planes on tensile fracture propagation in shale and tight sandstone. *Rock Mech Rock Eng*. <https://doi.org/10.1007/s00603-021-02742-2>
- Zoback MD, Kohli A, Das I, McClure M (2012) The importance of slow slip on faults during hydraulic fracturing stimulation of shale gas reservoirs. *Soc Petrol Eng–SPE Am Unconv Resour Conf* 2012(2011):344–352. <https://doi.org/10.2118/155476-ms>
- Zou Y, Ma X, Zhang S, Zhou T, Li H (2016) Numerical investigation into the influence of bedding plane on hydraulic fracture network propagation in shale formations. *Rock Mech Rock Eng* 49(9):3597–3614. <https://doi.org/10.1007/s00603-016-1001-5>

Publisher's Note Springer Nature remains neutral with regard to jurisdictional claims in published maps and institutional affiliations.

Springer Nature or its licensor (e.g. a society or other partner) holds exclusive rights to this article under a publishing agreement with the author(s) or other rightsholder(s); author self-archiving of the accepted manuscript version of this article is solely governed by the terms of such publishing agreement and applicable law.